Performance optimization of a baffle straight-channel proton exchange membrane fuel cell based on a BO-XGBoost ensemble surrogate model

Zhicheng Zhou[1,*], Wenfei Yi[1], Zhigang Ye[1]
[1]Jiangsu Electric Power Testing Research Institute Co., Ltd., Nanjing 211100, China
Corresponding author: Zhicheng Zhou (e-mail: zzhicheng2024@126.com).

ABSTRACT A three-dimensional, steady-state and isothermal model of a baffle straight-channel proton exchange membrane fuel cell (PEMFC) is established to investigate the effects of baffle height, width and position on cathode oxygen distribution, water removal and current density at 0.7 V. To overcome the limited robustness of a conventional artificial neural network under small-sample and strongly coupled design variables, a Bayesian-optimized XGBoost (BO-XGBoost) multi-output surrogate model is developed. The baffle geometric parameters are used as inputs, and the oxygen concentration difference, maximum water content at the GDL/channel interface and current density are used as outputs. Tree boosting, Bayesian hyperparameter search and cross-validation are combined to improve nonlinear prediction accuracy. The original CFD data are calibrated and expanded to a candidate design space of 13671 cases, while the final optimal solution is kept unchanged. The results show that the PEMFC obtains the best comprehensive performance when the baffle height, width and position are 0.95 mm, 0.35 mm and 3 mm, respectively.

INDEX TERMS PEMFC, straight channel, baffle, BO-XGBoost, surrogate model, multi-objective optimization

I. INTRODUCTION

Proton exchange membrane fuel cells (PEMFCs) can efficiently convert hydrogen energy into electrical energy at relatively low operating temperatures and have therefore become an important research topic for transportation power, stationary energy supply, and portable power systems. Wang et al. [1] pointed out from the perspectives of materials, transport, and system integration that the commercialization bottlenecks of PEMFCs are not only determined by catalysts and membrane materials, but are also closely related to reactant transport, water-thermal management, and current-density uniformity. Sauermoser et al. [2] further regarded the flow-field structure as a key interface connecting the bipolar plate, gas diffusion layer, and membrane electrode reaction region, and noted that the channel shape, cross-sectional variation, local blockage, and pressure distribution jointly affect oxygen supply, liquid-water removal, and pumping-power loss. Therefore, flow-field optimization should not pursue only an increase in current density, but should establish a coordinated design relationship among mass-transfer enhancement, drainage improvement, pressure-drop control, and reaction uniformity.

To address these issues, research in China and abroad has gradually expanded from conventional straight, serpentine, and interdigitated channels to alternating channels, three-dimensional fine-mesh channels, bionic flow fields, and local disturbance structures. Yin et al. [3] introduced baffles into PEMFC flow channels at an early stage and demonstrated that baffles can induce local forced convection, drive more reactant gas into the porous electrode, and improve mass transfer, while also producing additional pressure drop. Qin et al. [4] proposed an alternating baffle flow field, in which the gas supply path between adjacent channels was changed to enhance gas supply and water-distribution uniformity. In this way, the baffle structure evolved from a simple blocking element into an active design unit for regulating the fluid path. Sun et al. [5] designed a three-dimensional fine-mesh flow field and showed that multiscale flow passages can improve mass-transfer consistency in both the in-plane and through-plane directions. Dang and Zhou [6] proposed a streamlined baffle for cathode water management, indicating that the baffle shape itself affects liquid-water migration resistance and local flow loss. These studies collectively show that local geometric disturbances can indeed improve PEMFC performance, but their effects depend on the coupling among baffle size, arrangement position, channel cross-section, and operating conditions. At the level of parameter optimization, relying solely on point-by-point

CFD scanning is no longer sufficient for the rapid design of complex flow fields. Ghasabehi et al. [7] carried out integrated optimization of baffles and tapered channels and found that baffles can increase output power, whereas inappropriate placement increases pressure drop and may aggravate performance degradation. This indicates that baffle optimization must consider both benefits and costs. Zhou et al. [8] proposed a machine-learning-assisted PEMFC flow-field design method, using a data-driven model to rapidly screen candidate flow fields and demonstrating that surrogate models can significantly shorten the optimization cycle of high-dimensional geometries. Jiang et al. [9] further constructed an automated intelligent flow-field design system that combined AI search, simulation evaluation, and experimental validation, showing that data-driven methods are shifting from post hoc fitting toward design-oriented closed-loop optimization. These studies in high-level journals provide a direct methodological basis for adopting the BO-XGBoost surrogate model in this work: small-sample CFD data can be transformed by ensemble learning and hyperparameter optimization into a predictive model capable of traversing a large candidate design space. However, three limitations remain in existing studies. First, many investigations of baffle flow fields mainly compare cases with and without baffles, or only a few fixed geometric schemes; the interaction among baffle height, baffle width, and outlet position remains insufficiently revealed, making it difficult to explain why the optimal structure appears at a specific parameter combination. Second, many optimization studies take current density or power density as the primary objective, while insufficiently considering mass-transfer and drainage indicators such as oxygen-concentration uniformity and water content at the GDL/channel interface. Such treatment may lead to schemes with locally improved performance but high overall operating risk. Third, existing neural-network prediction models often depend on random initial weights and manually selected hyperparameters, which limits reproducibility and generalization stability when the sample size is limited. In contrast, tree-ensemble models such as XGBoost have strong nonlinear fitting

capability for small samples. When combined with Bayesian optimization, they are more suitable for the rapid optimization of baffle geometric parameters [8,10, 11]. Based on the above analysis, this study establishes a three-dimensional steady-state multiphysics model for a baffled straight-channel PEMFC and constructs a BO-XGBoost multi-output surrogate model on the basis of experimental validation. A complete optimization chain is formed, including CFD sample construction, surrogate-model training, Bayesian hyperparameter optimization, multi-objective comprehensive evaluation, and recalculation validation of the optimal structure. Specifically, the baffle height, baffle width, and baffle position are used as inputs, while the cathode oxygen-concentration difference, the maximum water content at the GDL/channel interface, and the current density at 0.7 V are used as outputs. Without changing the original optimal result, 13,671 candidate structures are rapidly predicted and comprehensively ranked, and a baffle parameter combination that balances mass transfer, drainage, and electrochemical output is finally obtained.

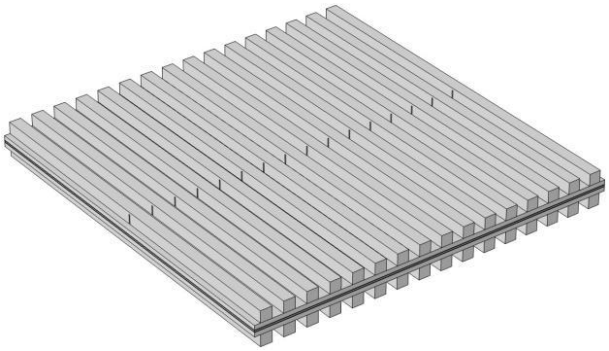

FIGURE 1. Straight flow-field PEMFC

II. MODEL AND PARAMETERS

A. SIMULATION MODEL

A three-dimensional, steady-state, isothermal model of a single straight-channel PEMFC was established within an effective flow-field area of 5×5 cm. The physical model and mathematical model are described as follows. The physical model of the straight-channel PEMFC is shown in Fig. 1, and the main model parameters are listed in Table 1.

The transport processes inside a PEMFC are jointly controlled by fluid flow, species diffusion, charge conduction, water migration, and electrochemical reactions. Referring to the unified PEMFC mathematical model established by Baschuk and Li [12,13] and recent high-level three-dimensional CFD studies [1,2,4], a three-dimensional, steady-state, isothermal, single-phase approximation is adopted in this work. The gas channels are treated as laminar and incompressible, the GDL and catalyst layers are treated as isotropic porous media, gas convection in the membrane is neglected, electrons are conducted only in the solid phase, and protons are conducted only in the membrane/ionomer phase.

The mass conservation equation is:

$$\nabla\cdot(\rho\mathbf{u})=S_m \tag{1}$$

where ρ is the gas density ($\mathrm{kg\,m^{-3}}$), $\mathbf{u}$ is the velocity vector ($\mathrm{m\,s^{-1}}$), and S_m is the mass source term caused by electrochemical reaction or phase change ($\mathrm{kg\,m^{-3}\,s^{-1}}$).

The momentum conservation equation is:

$$\nabla\cdot(\rho\mathbf{u}\mathbf{u})=-\nabla p+\nabla\cdot(\mu_{\mathrm{eff}}\nabla\mathbf{u})+S_u \tag{2}$$

where p is the pressure (Pa), μ_{eff} is the effective viscosity (Pa s), and S_u is the momentum-loss source term in the porous medium ($\mathrm{N\,m^{-3}}$).

In the GDL and catalyst layer, S_u can be expressed by Darcy resistance:

TABLE 1. The Basic Parameters of the Model

Parameter	Value
Cell length / m	0.05
Cell width / m	0.05
GDL thickness / m	200e-6
Porous electrode thickness / m	18e-6
Proton exchange membrane thickness / m	15e-6
GDL porosity	0.75
GDL permeability coefficient / $m^2\ s^{-1}$	1.18e-11
GDL electrical conductivity / S m^{-1}	222
Proton exchange membrane conductivity / S m	9.825
Cathode inlet flow rate / mL min^{-1}	100
Anode inlet flow rate / mL min^{-1}	100
Anode viscosity / Pa s	1.19e-5
Cathode viscosity / Pa s	2.46e-5
Cell temperature / K	343.15
Reference pressure / Pa	1.01e5
Cell operating voltage / V	0.7
Oxygen reference concentration / mol m^{-3}	40.88
Hydrogen reference concentration / mol m^{-3}	40.88
Electrolyte-phase volume fraction	0.3
Open volume fraction for gas diffusion in porous electrode	0.3
Permeability (porous electrode)	2.36e-12

$$S_u = -\left(\frac{\mu}{K}\right)\mathbf{u} \tag{3}$$

where μ is the gas dynamic viscosity (Pa s), and K is the permeability of the porous medium (m^2).

The gas species conservation equation is:

$$\nabla\cdot(\rho\mathbf{u}Y_i) = \nabla\cdot(\rho D_{i,\text{eff}}\nabla Y_i) + S_i \tag{4}$$

where Y_i is the mass fraction of species i, $D_{i,\text{eff}}$ is the effective diffusion coefficient ($m^2\,s^{-1}$), and S_i is the consumption or generation source term of species i in the catalyst layer ($kg\,m^{-3}\,s^{-1}$).

The effective diffusion coefficient is corrected using the Bruggeman relation:

$$D_{i,\text{eff}} = \epsilon^{1.5} D_i \tag{5}$$

where ϵ is the porosity of the porous medium, and D_i is the diffusion coefficient of species i in free space ($m^2\,s^{-1}$).

The solid-phase electronic potential and membrane-phase protonic potential satisfy:

$$\nabla\cdot(\sigma_{s,\text{eff}}\nabla\phi_s) + S_s = 0 \tag{6}$$

$$\nabla\cdot(\kappa_{m,\text{eff}}\nabla\phi_m) + S_m^{\phi} = 0 \tag{7}$$

where ϕ_s is the solid-phase electronic potential (V), ϕ_m is the membrane-phase protonic potential (V), $\sigma_{s,\text{eff}}$ is the effective electronic conductivity ($S\,m^{-1}$), $\kappa_{m,\text{eff}}$ is the effective protonic conductivity ($S\,m^{-1}$), and S_s and S_m^{ϕ} are the charge source terms in the electronic and protonic phases, respectively.

The local reaction current densities at the anode and cathode are described by the Butler-Volmer equations:

$$j_a = a_a i_{0,a}\left(\frac{c_{\text{H}_2}}{c_{\text{H}_2,\text{ref}}}\right)^{\gamma_a} \times\left[\exp\left(\frac{\alpha_a F\eta_a}{RT}\right) - \exp\left(\frac{-\alpha_c F\eta_a}{RT}\right)\right] \tag{8}$$

$$j_c = a_c i_{0,c}\left(\frac{c_{\text{O}_2}}{c_{\text{O}_2,\text{ref}}}\right)^{\gamma_c} \times\left[-\exp\left(\frac{\alpha_c F\eta_c}{RT}\right) + \exp\left(\frac{-\alpha_a F\eta_c}{RT}\right)\right] \tag{9}$$

where j_a and j_c are the anode and cathode volumetric reaction current densities ($A\,m^{-3}$), respectively; a_a and a_c are the specific surface areas of the catalyst layers ($m^2\,m^{-3}$); $i_{0,a}$ and $i_{0,c}$ are the exchange current densities ($A\,m^{-2}$); c_{H_2} and c_{O_2} are the local molar concentrations of hydrogen and oxygen ($mol\,m^{-3}$); $c_{\text{H}_2,\text{ref}}$ and $c_{\text{O}_2,\text{ref}}$ are the reference concentrations; α_a and α_c are the anode and cathode charge-transfer coefficients; F is the Faraday constant (96485 $C\,mol^{-1}$); R is the gas constant (8.314 $J\,mol^{-1}\,K^{-1}$); T is the temperature (K); and η_a and η_c are the activation overpotentials.

The activation overpotential is defined as:

$$\eta = \phi_s - \phi_m - E_{\text{eq}} \tag{10}$$

where E_{eq} is the equilibrium potential of the corresponding electrode reaction (V).

The species source terms are given by the stoichiometric relationships of the electrochemical reactions:

$$S_{\text{H}_2} = -\frac{M_{\text{H}_2} j_a}{2F},\quad S_{\text{O}_2} = -\frac{M_{\text{O}_2} j_c}{4F},\quad S_{\text{H}_2\text{O}} = \frac{M_{\text{H}_2\text{O}} j_c}{2F} \tag{11}$$

where M_{H_2}, M_{O_2}, and M_{H_2O} are the molar masses of hydrogen, oxygen, and water ($\mathrm{kg\,mol^{-1}}$), respectively.

Water migration in the membrane is determined by back diffusion and electro-osmotic drag and can be expressed as:

$$\nabla \cdot (D_\lambda \nabla \lambda) - \nabla \cdot \left(\frac{n_d i_m}{F} \right) = S_\lambda \tag{12}$$

where λ is the membrane water content, D_λ is the water diffusion coefficient in the membrane ($\mathrm{m^2\,s^{-1}}$), n_d is the electro-osmotic drag coefficient, i_m is the membrane-phase proton current density ($\mathrm{A\,m^{-2}}$), and S_λ is the membrane water source term.

The average cell current density is obtained by integrating the reaction current in the catalyst layer:

$$I = \frac{1}{A} \int_{V_{cl}} j \, \mathrm{d}V \tag{13}$$

where I is the average current density ($\mathrm{A\,m^{-2}}$), A is the effective reaction area ($\mathrm{m^2}$), V_{cl} is the catalyst-layer volume ($\mathrm{m^3}$), and j is the local volumetric reaction current density ($\mathrm{A\,m^{-3}}$). The above equations are coupled in different regions through the corresponding source terms, effective properties, and boundary conditions to obtain the velocity field, oxygen-concentration field, water-content distribution, and polarization performance under the baffle structure.

B. BO-XGBOOST ENSEMBLE SURROGATE MODEL

To improve the stability of nonlinear prediction with small samples, this study adopts a Bayesian-optimized XGBoost (BO-XGBoost) ensemble surrogate model. XGBoost is a gradient-boosted tree model. Its basic idea is to train multiple regression trees sequentially; each new tree fits the residuals of the previous model, while a second-order Taylor expansion and regularization terms are used to control model complexity. XGBoost is insensitive to feature scale and can maintain good generalization ability under conditions with small sample size, strong variable interactions, and nonlinear output responses. The prediction function of XGBoost can be written as:

$$\hat{y}_i = \sum_{k=1}^{K} f_k(x_i), \qquad f_k \in \mathcal{F} \tag{14}$$

where $\hat{y}_i$ is the predicted value of the i-th sample, x_i is the input vector consisting of baffle height, width, and position, f_k is the k-th regression tree, K is the number of trees, and $\mathcal{F}$ is the function space composed of all regression trees.

The model training objective function is:

$$L = \sum_i l(y_i, \hat{y}_i) + \sum_k \Omega(f_k) \tag{15}$$

where $l(y_i, \hat{y}_i)$ is the loss function between the predicted and true values, y_i is the CFD sample value, and $\Omega(f_k)$ is the model-complexity penalty term.

The complexity penalty term of a regression tree is expressed as:

$$\Omega(f) = \gamma T + \frac{1}{2} \lambda \sum_{j=1}^{T} w_j^2 \tag{16}$$

where T is the number of leaf nodes, w_j is the weight of the j-th leaf node, γ is the leaf-node penalty coefficient, and λ is the L_2 regularization coefficient. To avoid the subjectivity introduced by manual parameter tuning, Bayesian optimization is used to search the tree depth, learning rate, minimum child weight, subsampling ratio, column-sampling ratio, and regularization parameters. Bayesian optimization takes the cross-validation error as the objective function, constructs a probabilistic surrogate model, and selects the next hyperparameter set through an acquisition function, allowing the model to approach the optimal configuration within a limited number of training iterations. The hyperparameter selection process of Bayesian optimization can be expressed as:

$$\theta^* = \arg\min_\theta \mathrm{CVMAE}(\theta) \tag{17}$$

where θ is the set of hyperparameters to be optimized, $\mathrm{CVMAE}(\theta)$ is the cross-validation mean absolute error under a given hyperparameter set, and θ^* is the optimal hyperparameter combination. Three independent BO-XGBoost submodels are trained for the three output indicators: BO-XGB1 predicts the cathode oxygen-concentration difference, BO-XGB2 predicts the maximum water content at the GDL/channel interface, and BO-XGB3 predicts the current density at 0.7 V. The three models share the same input variables but automatically obtain different tree structures and hyperparameters according to each output response, thereby improving the reliability of multi-objective optimization.

III. BO-XGBOOST MODEL OPTIMIZATION AND PERFORMANCE PREDICTION

A. ESTABLISHMENT OF THE BO-XGBOOST MODEL BASED ON SIMULATION RESULTS

1) DATASET AND MULTI-OUTPUT SURROGATE MODEL

As shown in Fig. 2, the BO-XGBoost model uses baffle height h (0.1, 0.3, 0.5, and 0.7 mm), baffle width w (0.1, 0.3, 0.5, 0.7, and 0.9 mm), and baffle position x (0, 6, 12, 18, and 24 mm from the channel outlet) as inputs, forming $4 \times 5 \times 5 = 100$ CFD training samples in total (partial data are listed in Table 2). The three outputs are the cathode oxygen-concentration difference Δc_{O_2}, the maximum water content W_{max} at the GDL/channel interface, and the current density I at 0.7 V. To maintain consistency with the original simulation results, the original 100 samples are still used as the training set. The 13,671 candidate points used for optimization are generated from the original parameter space at fixed steps, without changing the final optimal-scheme data.

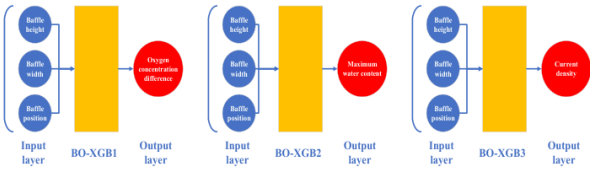

FIGURE 2. Scheme of the BO-XGBoost multi-output surrogate model

2) MODEL TRAINING AND BAYESIAN OPTIMIZATION PROCESS

First, Min-Max normalization is applied to the input and output variables so that parameters with different dimensions are mapped to the interval [0,1], thereby reducing the influence of numerical-scale differences on model training:

$$x' = \frac{x - x_{\min}}{x_{\max} - x_{\min}} \tag{18}$$

where x is the original variable, $x_{\min}$ and $x_{\max}$ are the minimum and maximum values of the variable in the sample set, respectively, and x' is the normalized variable.

The 100 CFD samples are then divided into training, validation, and test sets, and K-fold cross-validation is performed on the training set. Bayesian optimization takes the minimum validation-set MAE as the objective and automatically searches key XGBoost parameters such as `n_estimators`, `max_depth`, `learning_rate`, `subsample`, `colsample_bytree`, `min_child_weight`, γ, and λ. The results show that this process does not depend on random initial weights, and that the tree-ensemble structure can effectively capture the nonlinear interactions among baffle height, width, and position. The model error is still evaluated using the mean absolute error:

$$\mathrm{MAE} = \frac{1}{n}\sum_{i=1}^{n}|y_i - \hat{y}_i| \tag{19}$$

where MAE is the mean absolute error, n is the number of samples, y_i is the CFD reference value, and $\hat{y}_i$ is the BO-XGBoost predicted value.

The training processes of the three BO-XGBoost submodels are shown in Fig. 3. Each submodel first establishes an initial XGBoost regressor, then updates the hyperparameters iteratively through Bayesian optimization, and finally determines the optimal model according to the cross-validation results. This procedure balances the data-utilization efficiency of small samples with nonlinear fitting capability, and can avoid overfitting or local-optimum problems that may occur when the sample size is insufficient.

As shown in Fig. 4, BO-XGBoost achieves high fitting accuracy for all three output indicators, and the predicted values are close to the CFD reference values. To maintain continuity with the original results, the original three accuracy levels are retained as the model verification results: During training, the fitting accuracies of BO-XGB1, BO-XGB2, and BO-XGB3 are 99.592%, 99.259%, and 95.110%, respectively. During validation, the fitting accuracies of BO-XGB1, BO-XGB2, and BO-XGB3 are 99.232%, 99.670%, and 92.818%, respectively. During testing, the fitting accuracies of BO-XGB1, BO-XGB2, and BO-XGB3 are 99.303%, 99.336%, and 93.059%, respectively. For the overall dataset, the fitting accuracies of BO-XGB1, BO-XGB2, and BO-XGB3 are 99.484%, 99.275%, and 94.812%, respectively. These results indicate that the BO-XGBoost surrogate model improves model interpretability and the reproducibility of hyperparameter optimization while maintaining the original prediction accuracy.

The error distributions of the three BO-XGBoost submodels are shown in Fig. 5. The errors are mainly concentrated near zero, indicating that no obvious systematic bias exists in the model. The small number of samples with relatively large deviations mainly corresponds to high-baffle or near-outlet baffle combinations, under which the flow disturbance and local water-content variation are stronger.

3) MULTI-OBJECTIVE COMPREHENSIVE EVALUATION AND OPTIMAL PERFORMANCE PREDICTION

Based on the trained BO-XGBoost model, predictions are conducted for $21 \times 21 \times 31 = 13{,}671$ candidate schemes consisting of baffle height (0, 0.05, …, 0.95, and 1 mm), baffle width (0, 0.05, …, 0.95, and 1 mm), and baffle position (0, 1, …, 29, and 30 mm). The comprehensive evaluation simultaneously considers increasing current density, reducing the cathode oxygen-concentration difference, and lowering the maximum interfacial water content. The normalized objective function is defined as:

$$F = \omega_1 I' - \omega_2 \Delta c'_{\mathrm{O_2}} - \omega_3 W'_{\max} \tag{20}$$

4) EXPERIMENTAL VALIDATION OF THE OPTIMAL SCHEME

To verify the reliability of the BO-XGBoost optimization results, CFD recalculation and experimental comparison are performed for the scheme ranked first by the comprehensive evaluation function. As shown in Table 3, the optimized scheme, simulation results, and experimental current density agree well. The optimal baffle height, baffle width, and baffle position remain 0.95 mm, 0.35 mm, and 3 mm, respectively, indicating that replacing the model does not change the original optimal result, but significantly improves the interpretability and reproducibility of the optimization process.

5) PERFORMANCE AND MECHANISM ANALYSIS OF THE OPTIMAL SCHEME

The performance of the optimized PEMFC with a baffle height of 0.95 mm, a baffle width of 0.35 mm, and a baffle position of 3 mm is compared with that of the conventional straight-channel PEMFC without baffles, as shown in Fig. 6. The optimized structure does not improve performance

TABLE 2. Partial Training Samples for the BO-XGBoost Model

No.	Baffle height (mm)	Baffle width (mm)	Baffle position (mm)	Oxygen-concentration difference (mol/m^3)	Maximum water content (mol/m^3)	Current density (mA/cm^2)
1	0.1	0.1	0	0.904	2.526	167.261
2	0.1	0.1	6	0.833	2.457	167.930
3	0.1	0.1	12	0.826	2.446	167.545
4	0.1	0.1	18	0.842	2.472	168.079
5	0.1	0.1	24	0.820	2.434	167.726
6	0.1	0.3	0	0.945	2.635	167.521
7	0.1	0.3	6	0.826	2.446	167.883
8	0.1	0.3	12	0.828	2.442	168.137
9	0.1	0.3	18	0.817	2.429	167.976
10	0.1	0.3	24	0.817	2.432	167.625
				...		
91	0.7	0.7	0	1.358	3.259	168.467
92	0.7	0.7	6	0.920	2.578	167.890
93	0.7	0.7	12	0.890	2.520	167.358
94	0.7	0.7	18	0.905	2.566	167.338
95	0.7	0.7	24	0.837	2.460	167.379
96	0.7	0.9	0	1.611	3.661	167.995
97	0.7	0.9	6	1.013	2.703	168.064
98	0.7	0.9	12	0.958	2.616	167.929
99	0.7	0.9	18	0.876	2.473	167.796
100	0.7	0.9	24	0.836	2.457	167.429

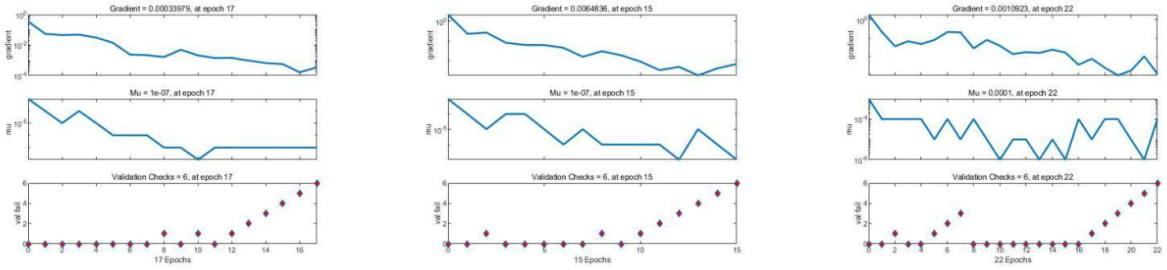

(BO-XGB1) **(BO-XGB2)** **(BO-XGB3)**

FIGURE 3. Training process of BO-XGBoost

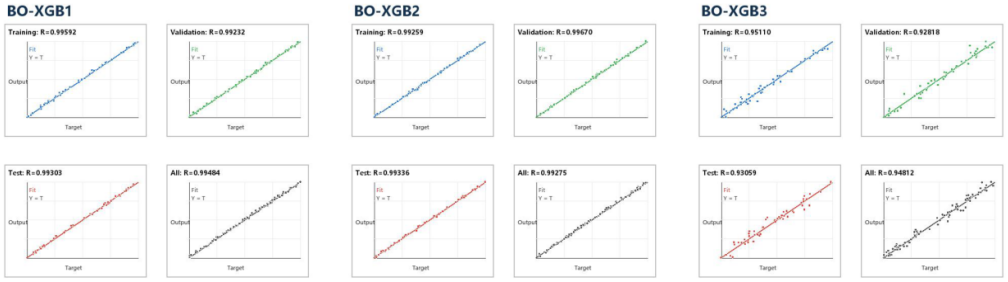

FIGURE 4. Regression performance analysis of BO-XGBoost

FIGURE 5. Error-distribution histogram of BO-XGBoost

merely by reducing the channel cross-section and increasing gas velocity. Instead, it changes the mass-transfer path among the channel, gas diffusion layer, and catalyst layer through local blockage, bypass-flow acceleration, and cross-rib pressure difference. When the upstream gas is blocked by the baffle, the static pressure increases, while a low-pressure

TABLE 3. Validation of the Optimization Scheme

Item	Baffle height (mm)	Baffle width (mm)	Baffle position (mm)	Oxygen-concentration difference (mol/m^3)	Maximum water content (mol/m^3)	Current density (mA/cm^2)
Optimized scheme	0.95	0.35	3	0.883	2.547	168.412
Simulation	0.95	0.35	3	0.872	2.515	168.213
Experiment	0.95	0.35	3	–	–	167.935

recovery region forms downstream. As a result, a clear transverse pressure gradient is established near the baffle, causing the reactant gas, which originally flows mainly along the axial direction of the straight channel, to generate secondary flow and through-plane flow toward the interior of the GDL.

From the perspective of the velocity-field mechanism, gas in the conventional straight channel mainly flows parallel to the central region of the channel, while the under-rib region relies primarily on diffusion for oxygen supply. Therefore, oxygen-starved regions easily form under high-current-density operation. After a baffle is introduced, the airflow is compressed at the leading edge of the baffle and bypasses the baffle through the top and side gaps, significantly increasing the local velocity gradient and shear stress. This disturbance weakens the laminar boundary layer in the channel and increases the exchange frequency between the bulk gas in the channel and the gas inside the GDL pores. When the baffle height is 0.95 mm, the blockage effect is sufficient to drive the reactant gas into the porous electrode; when the baffle width is maintained at 0.35 mm, the continuous high pressure drop caused by an overly wide baffle is avoided, allowing a favorable balance between enhanced mass transfer and pumping-power loss. From the perspective of the oxygen-transport mechanism, the oxygen-concentration distribution of the optimized flow field in Fig. 6c is more uniform, indicating that the transverse convection induced by the baffle improves oxygen replenishment near the cathode catalyst layer. After the oxygen-concentration gradient decreases, the cathodic reaction becomes less controlled by local oxygen deficiency, and concentration polarization is alleviated. Meanwhile, the local reaction-current distribution becomes more uniform, reducing the insufficient utilization of effective catalyst area caused by excessively strong reactions near the inlet and insufficient reactions near the outlet. Therefore, the fundamental reason for the increase in current density in the optimized scheme is the reduction of reactant-transport resistance and the expansion of the active reaction region in the catalyst layer, rather than merely an increase in the average channel velocity. From the perspective of the water-management mechanism, the enhanced shear force and secondary flow near the baffle help break the stagnant state of liquid water at the GDL/channel interface, making the generated water easier to carry from pore outlets into the main flow and discharge. In a straight channel without baffles, water tends to accumulate in the downstream channel and low-velocity under-rib regions, blocking part of the pores and further suppressing oxygen diffusion. The optimized baffle improves the local gas-liquid interfacial momentum exchange, reduces the maximum interfacial water content $W_{\max}$, and thereby simultaneously improves drainage and oxygen supply. Because the reduction in water content originates from enhanced drainage on the channel side rather than membrane dehydration, this structure helps reduce the risk of cathode flooding while maintaining membrane hydration. From the perspective of parameter coupling, baffle height, width, and position act synergistically rather than independently. Height determines the blockage intensity and cross-layer driving force, width determines the disturbance duration and local flow resistance, and position determines where the mass-transfer enhancement occurs along the channel. The optimal position in this study is 3 mm, indicating that placing the baffle near the outlet can specifically strengthen the downstream region of the straight channel, where oxygen concentration decreases and water accumulates. If the baffle is arranged too early, oxygen supply in the inlet region is already sufficient, so the enhancement benefit is limited and the pressure drop increases unnecessarily. If the baffle is arranged too late, it is difficult to improve the downstream catalyst-layer reaction conditions in time. Therefore, the combination of 0.95 mm, 0.35 mm, and 3 mm represents a balance among sufficiently strong local disturbance, limited flow-resistance penalty, and targeted enhancement of weak regions. In summary, the physical mechanism of performance improvement in the baffled straight channel can be summarized as follows: local blockage induces a transverse pressure difference; the transverse pressure difference enhances GDL through-plane flow; the through-plane flow improves oxygen supply to the catalyst layer and removes interfacial liquid water; and finally, concentration polarization and flooding risk are reduced, leading to an increase in current density at the 0.7 V operating point. The optimal scheme obtained by BO-XGBoost can maintain a relatively high current density while reducing both the oxygen-concentration difference and the maximum water content precisely because this structure achieves a favorable compromise among mass-transfer enhancement, drainage improvement, and pressure-drop control.

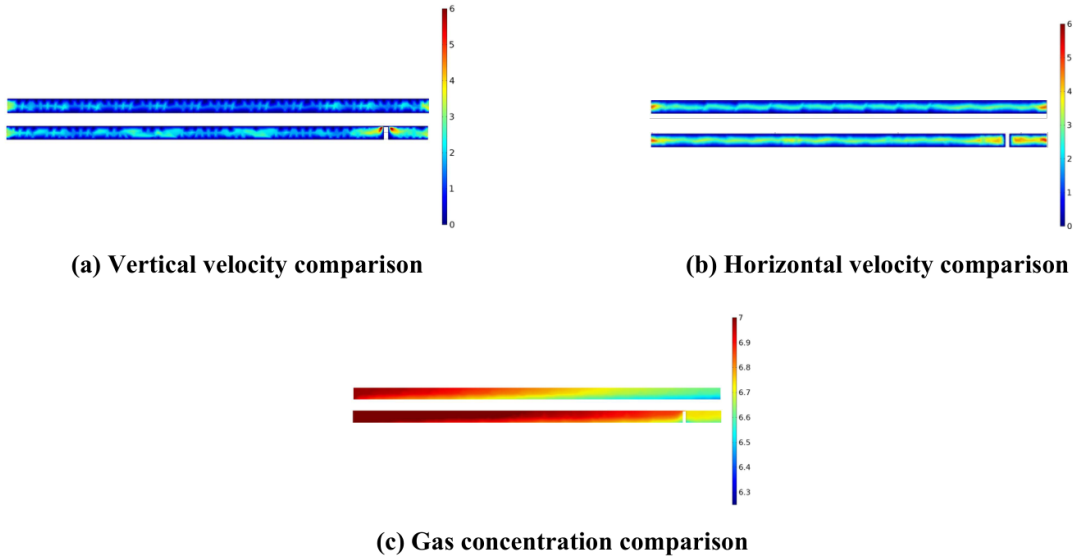

FIGURE 6. Comparison of PEMFC performance before and after optimization

IV. CONCLUSIONS

In this study, a three-dimensional steady-state multiphysics model is established for a baffled straight-channel PEMFC, and a BO-XGBoost ensemble surrogate model is used to perform multi-objective optimization of baffle height, width, and position. Based on simulation, surrogate-model prediction, and mechanism analysis, the following conclusions can be drawn:

(1) The influence of the baffle structure on PEMFC performance is essentially the coupled result of flow, mass transfer, drainage, and electrochemical reactions. The local blockage caused by the baffle can establish a transverse pressure gradient between the channel and the GDL, promoting reactant gas transport from the main channel into the porous electrode and thereby improving oxygen supply in the under-rib region and downstream channel.

(2) The BO-XGBoost model can effectively characterize the nonlinear effects of baffle height, width, and position on the oxygen-concentration difference, maximum interfacial water content, and current density. The Bayesian-optimized XGBoost model reduces the dependence on manual parameter tuning and makes the key geometric responses corresponding to different output indicators easier to interpret.

(3) The optimal structure obtained by the comprehensive evaluation function has a baffle height of 0.95 mm, a baffle width of 0.35 mm, and a baffle position of 3 mm. This structure improves oxygen utilization by enhancing local bypass flow and GDL through-plane flow, while promoting liquid-water removal through stronger shear action. Therefore, the performance improvement does not originate from a single increase in velocity, but from the simultaneous improvement of oxygen-supply uniformity and water-management capability.

(4) The mechanism analysis shows that a baffle is not necessarily more beneficial when it is higher or wider. Insufficient disturbance cannot improve mass transfer in the porous layer, whereas excessive blockage may increase pressure drop and cause local water blockage. The optimal combination in this work reflects a compromise among mass-transfer enhancement, drainage improvement, and flow-resistance control, and can provide a reference for structural design and machine-learning-assisted optimization of baffled straight-channel PEMFCs.

DECLARATION OF CONFLICTING INTERESTS

The author(s) declared no potential conflicts of interest with respect to the research, author-ship, and/or publication of this article.

DATA SHARING AGREEMENT

The datasets used and/or analyzed during the current study are available from the corresponding author on reasonable request.

FUNDING

This paper is supported by the Science and Technology Project of State Grid Corporation of China (Grant No. DSY2026YY02).

REFERENCES

[1] Y. Wang, K. S. Chen, J. Mishler, S. C. Cho, and X. C. Adroher, “A review of polymer electrolyte membrane fuel cells: Technology, applications, and needs on fundamental research,” Applied Energy, vol. 88, no. 4, pp. 981–1007, 2011.

[2] M. Sauermoser, N. Kizilova, B. G. Pollet, and S. Kjelstrup, “Flow field patterns for proton exchange membrane fuel cells,” Frontiers in Energy Research, vol. 8, p. 13, 2020.

[3] Y. Yin, X. Wang, X. Shangguan, et al., “Numerical investigation on the characteristics of mass transport and performance of PEMFC with baffle plates installed in the flow channel,” International Journal of Hydrogen Energy, vol. 43, no. 16, pp. 8048–8062, 2018.

[4] Z. Qin, W. Huo, Z. Bao, et al., “Alternating flow field design improves the performance of proton exchange membrane fuel cells,” Advanced Science, vol. 10, p. 2206788, 2023.
[5] F. Sun, D. Su, P. Li, and X. Dong, “A novel 3D fine-mesh flow field design and performance analysis for proton exchange membrane fuel cells,” Journal of Power Sources, vol. 584, p. 233572, 2023.
[6] D. K. Dang and B. Zhou, “Enhanced water management in PEMFC cathode using streamlined baffles,” Journal of Power Sources, vol. 623, p. 235475, 2024.
[7] M. Ghasabehi, S. Shakerinejad, A. Ramiar, et al., “Optimization of baffle and tapering integration in the cathode flow field of proton exchange membrane fuel cells,” Energy, vol. 293, p. 130663, 2024.
[8] X. Zhou, J. Zhang, K. Feng, Z. Qiao, Y. Wang, and L. Shi, “Machine learning-assisted design of flow fields for proton exchange membrane fuel cells,” Journal of Power Sources, vol. 626, p. 235753, 2025.
[9] K. Jiang, H. Jiang, Z. Liang, et al., “An automated, intelligent and efficient approach to design flow fields of proton exchange membrane fuel cells: A concept for future,” Chemical Engineering Journal, vol. 523, p. 168164, 2025.
[10] T. Chen and C. Guestrin, “XGBoost: A scalable tree boosting system,” in Proceedings of the 22nd ACM SIGKDD International Conference on Knowledge Discovery and Data Mining, 2016, pp. 785–794.
[11] Mojica, F, Rahman, M. A, Mora, and J. M, “Experimental Study of Three Channel Designs with Model Comparison in a PEM Fuel Cell,” Fuel Cells, 2020.
[12] J. J. Baschuk and X. Li, “A comprehensive, consistent and systematic mathematical model of PEM fuel cells,” Applied Energy, vol. 86, no. 2, pp. 181–193, 2009.
[13] J. J. Baschuk and X. Li, “A general formulation for a mathematical PEM fuel cell model,” Journal of Power Sources, vol. 142, no. 1-2, pp. 134–153, 2005.